NUMERICAL SENSITIVITY ANALYSIS OF MATERIAL PARAMETERS IN TIG WELDING ARC MODELLING

M. LE GAL LA SALLE*,**, S. CADIOU**, M. COURTOIS**, M. CARIN**, A. BROSSE**

**Framatome, 69007, Lyon, France*
***Univ. Bretagne Sud UMR CNRS 6027 IRDL, 56100, Lorient, France*

DOI 10.3217/978-3-99161-089-2-002, license CC BY 4.0

ABSTRACT

The simulation of the TIG/GTAW process with arc-melt pool coupling involves several material properties that are not well known. The main goal of this study is to quantify the numerical sensitivities of these arc material properties on the melt pool behaviour and provide recommendations on influential parameters. The most sensitive properties are thermal conductivity, density, heat capacity and viscosity of argon. For instance, a 10% increase in C_p can result in an increase of more than 23% in the melt pool volume. This sensitivity study includes a detailed presentation of the 2D axisymmetric magneto-thermo-hydrodynamic finite element simulation developed with a dynamic coupling between the arc and melt pool and free surface deformation of the plasma-anode interface.

Keywords: GTAW, TIG, magneto-thermo-hydrodynamic, arc, melt-pool

INTRODUCTION

Numerical modelling of the TIG process is a relatively recent subject of research. One of the founding models is probably the works of Hsu and Pfender [1] when he produced a magneto-thermo-hydrodynamic model of the arc in a stationary regime and in an axisymmetric configuration. His model is applied to currents between 100 and 300 A and arc heights between 10 and 20 millimetres. This numerical work is associated with experimental temperature measurements by spectrometry, with two objectives. First, to adjust the material parameters associated with electron emission and ion neutralization at the surface of the tungsten electrode. Secondly, to quantify the predictivity of the numerical results. These numerical and experimental results are enriched by the work of McKelliget and Szekely [2].

Hsu noted the sensitivity of the electromagnetic resolution near the cathode. This was the subject of work by Lowke et al. [3], who developed a methodology to simulate the transition between the cathode and the plasma without taking into account ambipolar diffusion and performed a mesh decoupling between thermo-hydrodynamics and electromagnetics. Recently, a model focusing solely on the arc was studied by Velázquez-Sánchez et al. [4] to better understand the mechanisms dominating heat transfer. Maps were thus proposed to locate the dominant heat input and output in the different areas of the arc. In parallel with the work on the arc, the modelling of the melt pool has been the subject of numerous studies involving an approximation of the effect of the arc by electromagnetic, thermal and hydrodynamic source terms. The work of Oreper et al. [5], Szekely et al. [6], Zacharia et al. [7], Choo et al. [8], and Debroy et al. [9] are based on this methodology, providing an improved understanding of the phenomena inside the melt pool.

Subsequently, arc-melt pool coupling was developed in 2D axisymmetric configuration with, for example, the work of Lin et al. [10] integrating a stationary simulation of the arc and the melt pool with surface deformation. This model was used by Kim et al. [11] to study the effect of current pulsation on melt pool behaviour. A reference model is the work of Tanaka et al. [12] for which multiple iterative developments have been carried out, such as the consideration of metal vapours in the arc coming from the melt pool with Murphy et al. [13]. Recently, Brochard [14] resumed the development of this model. He developed the justification and analysis of the multiple assumptions with an experimental comparison focused on the heat absorbed by the anode. Traidia et al. [15] added to the model the deformation of the interface between the plasma and the melt pool which is a very important element to consider at high intensities. The deformation of the surface under the effect of the arc pressure is calculated by an approach that minimizes its mechanical energy by the Helmholtz equation. This model was used to quantify the influence of the shielding gas and the effect of current pulsations. In addition to this work on the 2D axisymmetric model, a methodology was developed to project the results into 3D. This hybrid approach enables the simulation of the melt pool with slow torch advance, which is a major step forward. More recently the 2D axisymmetric model of Nahed et al. [16] integrated an arc-melt pool coupling with a deformable surface. He used a local kinematic and dynamic coupling, which is more physical than the global energy approach. A sensitivity study was conducted with this model to improve the understanding of the electrode sharpening. A fully 3D model of the arc and melt pool with a non-deformable interface was produced. The recent work of Ebrahim et al. [17] and Wu et al. [18] are an example of applications at the industrial process scale. Other more fundamental work studies the modelling of radiative transfers within the arc such as those of Baeva et al. [19], or the effect of metal vapours like Wang et al. [20].

In the nuclear industry, the welding process is used to assemble large steel components. To improve control of the process, numerical simulation of TIG/GTAW (Tungsten Inert Gas/Gas Tungsten Arc Welding), and more specifically of the electric current pulsation cycles, is being developed to develop the understanding of the physical phenomena and their influence on the melt pool, including: welding difficulties (lack of penetration, migration of chemical species, etc.), and effects of process parameters (electric current, torch speed). A magneto-thermo-hydrodynamic model with surface deformation and melt pool-arc coupling in a 2D axisymmetric configuration is developed. This model requires several material parameters for

which limited data is available in the literature, which explains why all previously cited modeling studies relied on the same dataset. These properties are difficult to characterize, especially at high temperatures and based either on thermodynamics analyses or global estimation by inverse methods. Due to the inability to estimate all the variabilities associated with these properties, a sensitivity study is performed to quantify their effects on the melt pool and present an importance analysis. This arc-scale sensitivity study for this specific configuration has not been the subject of any previous work in the literature with a coupling between arc material properties and consequences on the melt pool. These numerical results can be used to justify the necessity of improving the understanding of phenomena that can modify the material properties of the plasma, such as metallic vapor. This study is performed at an arc length of 2 mm, which is closer to the industrial application of the process compared to other works : 5 mm [13], 7 mm [4], 10 mm [1].

The first part of this article provides a comprehensive description of the model, developed with the COMSOL Multiphysics® software, including: a description of the process and the associated physical phenomena, the geometry used in the simulation, the mathematical formulation, the presentation and justification of the associated assumptions, the material properties used, the spatial discretization and the numerical model used. The second part is focused on the numerical analysis, including: a general presentation of the results at the scale of the arc and melt pool, an energy balance of the phenomena involved, and a sensitivity analysis of the material properties.

MAGNETO-THERMO-HYDRODYNAMIC SIMULATION OF THE TIG PROCESS

PROCESS PRESENTATION AND PHENOMENA INVOLVED

The TIG/GTAW (Tungsten Inert Gas/Gas Tungsten Arc Welding) process is an arc welding method. An electrical arc is formed between an infusible tungsten cathode and an anode consisting of the metal welded. The interstitial medium is a plasmagenic gas such as argon or helium. The heat generated by the arc leads to a localised fusion of the metal. The main physical phenomena in arc welding are electromagnetism, heat transfer, fluid flow, solid mechanics, and metallurgy. The goal of our work is to improve the understanding of the melt pool that is why we study only the physics that have a significant impact on the melt pool: electromagnetism, heat transfer and fluid flow. The right of the figure 1 summarises all the phenomena in the arc and the melt pool.

GEOMETRY

The configuration studied is a static fusion spot on a stainless steel (304L) cylinder with no filler metal. The weld is made in the center of its upper face. This part is placed on a device developed to have as much as possible dissipation only in convection and radiation. The device is designed to achieve relative axisymmetry of the electromagnetic field. A tungsten electrode

with 2% of thorium is used. The shielding gas is argon (ARCAL™ PRIME) with 99.995% purity according to the supplier. It is blown through a straight ceramic nozzle. The left of the figure 1 is an illustration of the simulated configuration.

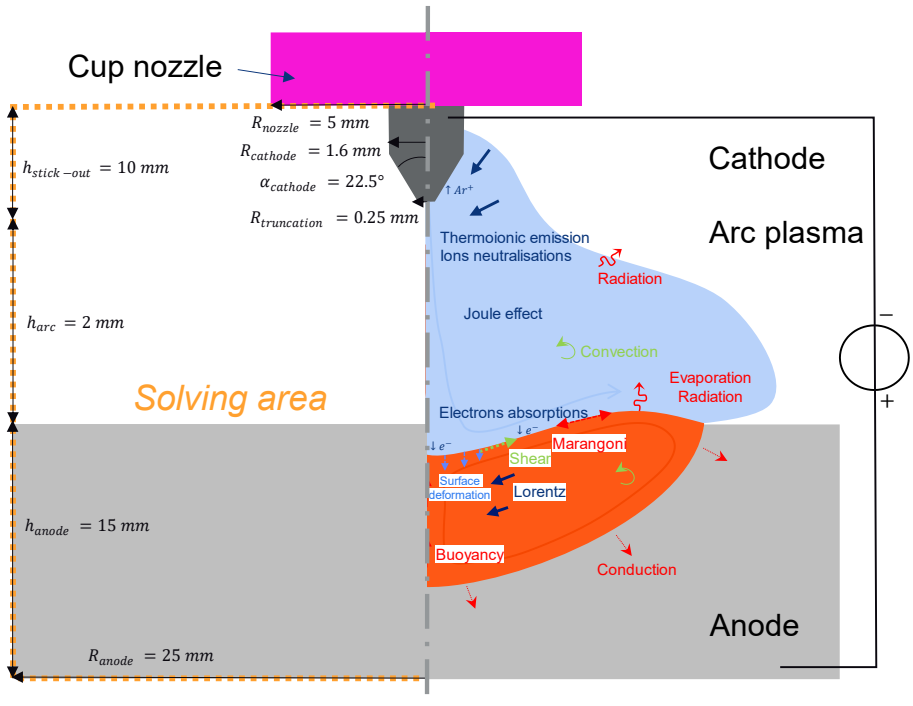

Fig. 1 Illustration of the phenomena present and the geometry (not at scale) of the TIG process

MATHEMATICAL FORMULATION

Nomenclature

$\vec{A}$	Magnetic vector potential	$\vec{n}$	Normal vector
A_r	Richardson constant	∇_s	Surface divergence
B	Darcy's law coefficient	p_1	Pressure in plasma
$\vec{B}$	Magnetic flux density	p_2	Pressure in anode
C	Darcy's law coefficient	ϕ	Axial displacement of the mesh
C_p	Heat capacity at constant temperature	ϕ_a	Work function at the anode interface
e	Elementary charge	ϕ_e	Work function associated with thermoionic emission

$\vec{E}$	Electric field	ϕ_c	Work function at the cathode interface
ϵ	Net emissivity	ψ	Axial displacement of the interface anode-plasma
ϵ_a	Anode surface emissivity	$\vec{q}$	Heat flux vector
ϵ_c	Cathode surface emissivity	Q_{anode}	Total heat flux at anode surface
fl	Liquid fraction of metal	σ	Electrical conductivity
$\vec{g}$	Acceleration of gravity	σ_B	Stefan-Boltzmann constant
γ	Surface tension coefficient for Marangoni	$\overline{\overline{\sigma_1}}$	Stress viscous tensor of plasma
γ^*	Equivalent surface tension coefficient for interface deformation	$\overline{\overline{\sigma_2}}$	Stress viscous tensor of anode
γ_l	Equivalent surface tension coefficient for interface deformation	ρ	Density
γ_s	Equivalent surface tension coefficient at solid state for metal	ρ_{ref}	Reference density for thermal expansion of liquid metal
$\vec{H}$	Magnetic density	s_{vap}	Vaporisation source term
h_{conv}	Convection coefficient	T	Temperature
I_0	Input intensity	$\vec{t}$	Tangential vector
$\vec{J}$	Current density vector	T_{ref}	Reference temperature for thermal expansion of liquid metal

This formulation is inspired and compared with the work of Hsu et al. [1], Tanaka et al. [12], Brochard [14], Traidia et al. [15], Cadiou et al. [21] and Nahed et al. [16] whose arc models are compared to the experimental data of Hsu et al. [1] as shown in the appendix by figures 12 and 13. This simulation involves multiple equations associated with:

- Three physics: electromagnetism, fluid flow in plasma and metal, and heat transfer.
- Plasma-anode interface deformation: Helmholtz's equation for minimising the associated energy and modified Laplace's equation to move the surrounding mesh.

The equations associated with this model are detailed for each physical, but for simplicity, the axisymmetric conditions are not included. These equations apply to the geometric domains and boundaries as shown in figure 2. Figure 3 summaries the couplings between these different equations.

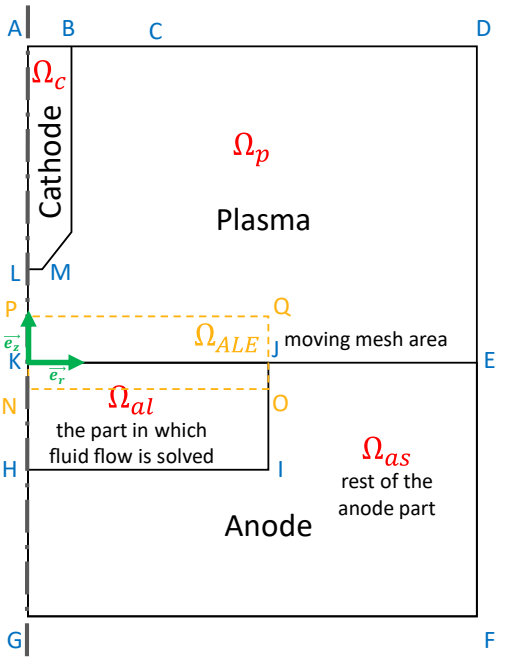

Fig. 2 Solving domains

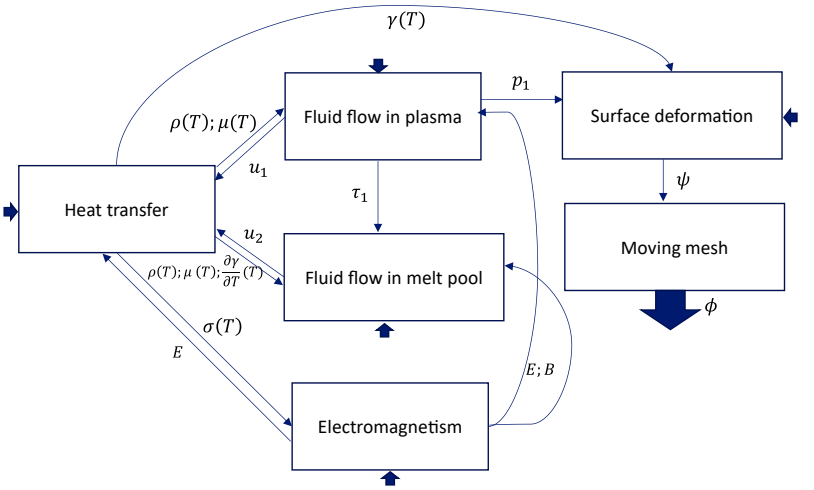

Fig. 3 Schematic representation of the couplings between equations

Electromagnetism ($\Omega_c \cup \Omega_p \cup \Omega_{al} \cup \Omega_{as}$)

The electromagnetic field in cathode, plasma and anode is described by Ampere's law (4), Ohm's law (5) and Faraday's law (6) under static conditions. A Lorentz gauge is introduced by equation (7) to ensure the uniqueness of the solution. At the top of the tungsten electrode ($\partial\Omega\epsilon AB$), the surface integral of the current density is imposed by the equation (8), with I_0 as the input intensity. The nullity of the electric potential is defined by equation (9) on the underside of the cylinder ($\partial\Omega\epsilon GF$), where the ground is connected. Electromagnetic isolation conditions are imposed by equations (10) and (11) on the outer boundaries of the domain ($\partial\Omega\epsilon BD \cup DF \cup FG$), with $\vec{n}$ as the normal vector of these boundaries.

$$\vec{B} = \nabla \times \vec{A} \tag{1}$$

$$\vec{B} = \mu_r \mu_0 \vec{H} \tag{2}$$

$$\vec{E} = -\nabla V \tag{3}$$

$$\nabla \times \vec{H} = \vec{J} \tag{4}$$

$$\vec{J} = \sigma \vec{E} \tag{5}$$

$$\nabla . \vec{J} = 0 \tag{6}$$

$$\nabla . \vec{A} = 0 \tag{7}$$

$$\int_{AB} -\vec{J} . \overrightarrow{e_z} dS = I_0 \tag{8}$$

$$V = 0 \tag{9}$$

$$\vec{n} . \vec{J} = 0 \tag{10}$$

$$\vec{n} \times \vec{A} = \vec{0} \tag{11}$$

j_c corresponds to the normal current leaving the cathode at cathode-plasma interface ($\partial\Omega_c \cap \partial\Omega_p$). It includes two distinct phenomena: j_{em}, which corresponds to a flow of electrons associated with the thermionic effect (15) using Richardson's law (13) and j_{ion}, which corresponds to the neutralisation of ions at the cathode-plasma interface (14). These two current densities later used to consider the associated thermal phenomena.

$$j_c = \vec{J} . \overrightarrow{n_{cathode \rightarrow plasma}} \tag{12}$$

$$j_{em} = A_r T^2 \, exp\left(-\frac{e\phi_e}{k_B T}\right) \tag{13}$$

$$j_{ion} = \begin{cases} j_c - j_{em} \; for \; j_c - j_{em} > 0 \\ 0 \; otherwise \end{cases} \tag{14}$$

$$j_e = j_c - j_{ion} \tag{15}$$

Heat transfer ($\Omega_c \cup \Omega_p \cup \Omega_{al} \cup \Omega_{as}$)

The heat equation (16) is solved over the entire domain in its temporal form, including source terms associated with the Joule effect and plasma radiation losses with partial self-absorption (18). The temperature at the top of the tungsten electrode ($\partial\Omega \in AB$) is imposed by equation (19), reflecting the cooling of the torch. At the periphery of the plasma ($\partial\Omega \in BD \cup DE$), a convection loss generated by the fluid outlet is considered, which is why conduction is considered null (20). At the anode boundary ($\partial\Omega \in EF \cup FG$), a loss by convection and radiation is defined by equation (21).

$$\rho C_p \frac{\partial T}{\partial t} + \rho C_p \vec{u}.\nabla T + \nabla.\vec{q} = S \tag{16}$$

$$\vec{q} = -\lambda \times \nabla T \tag{17}$$

$$S = \begin{cases} \vec{J}.\vec{E} - 4\pi\epsilon \; for \; \Omega \in \Omega_p \\ \vec{J}.\vec{E} \; for \; \Omega \in \Omega_{al} \cup \Omega_{as} \cup \Omega_c \end{cases} \tag{18}$$

$$T = T_0 \tag{19}$$

$$\vec{q}.\vec{n} = 0 \tag{20}$$

$$-\vec{n}.\vec{q} = h_{conv} \times (T_0 - T) + \epsilon_a \sigma_B \times (T_0^4 - T^4) \tag{21}$$

At the cathode-plasma interface ($\partial\Omega \in \Omega_\mathrm{p} \cap \Omega_\mathrm{c}$), the flux is defined by equation (22) with the heat input generated by ion neutralisation and heat sink due to thermoionic emission and radiation. At the anode-plasma interface ($\partial\Omega \in (\partial\Omega_\mathrm{p} \cap (\partial\Omega_\mathrm{al} \cup \partial\Omega_\mathrm{as}))$), the flux defined by the equation (23) includes the heat input generated by electron absorption, losses due to radiation and vaporization. The term associated with this last phenomenon is derived from Debroy et al. [22] and is defined by equation (24), using the iron vapour pressure from Kim et al. [23].

$$-\vec{n}.\vec{q} = j_{ion} V_i - j_e \phi_c - \epsilon_c \sigma_B T^4 \tag{22}$$

$$-\vec{n}.\vec{q} = \vec{J}.\vec{n}\phi_a - \epsilon_a \sigma_B T^4 - s_{vap} \tag{23}$$

$$s_{vap} = -10^{\left(2.52+\left(6.121-\frac{18836}{T}\right)-0.5\log_{10}(T)+1\right)} \times L_{vap} \tag{24}$$

Fluid flow in plasma (Ω_p)

In the plasma domain (Ω_p), equations (25) and (26) define the conservation of mass and momentum, incorporating the Lorentz force and gravity. The viscous stress tensor for a weakly compressible flow is defined by equation (27). A pressure condition is imposed at point D to ensure the uniqueness of the solution by equation (28). The velocity is considered null at the boundary with anode and cathode ($\partial\Omega \in (\partial\Omega_\mathrm{p} \cap (\partial\Omega_\mathrm{al} \cup \partial\Omega_\mathrm{as} \cup \partial\Omega_\mathrm{c}))$, according to equation (29). An open boundary condition is defined by the nullity of the viscous term at

($\partial\Omega \in (\mathrm{CD} \cup \mathrm{DE})$), as stated in equation (30). The inlet of the shielding gas is governed by the Poiseuille's law, leading to equation (31). The axial displacement of the plasma-anode interface ($\partial\Omega \in (\partial\Omega_\mathrm{p} \cap \partial\Omega_\mathrm{a})$) is equal to ψ involving normal and tangential velocity conditions defined by equations (32) and (33). Note that gravity is taken into account in equation (26) but could be neglected due to its minor contribution.

$$\frac{\partial \rho}{\partial t} + \nabla.(\rho\overrightarrow{u_1}) = 0 \tag{25}$$

$$\rho\left(\frac{\partial \overrightarrow{u_1}}{\partial t} + (\overrightarrow{u_1}.\nabla)\overrightarrow{u_1}\right) = \nabla.\left(-p_1\bar{\bar{I}} + \bar{\bar{\sigma}}\right) + \vec{J} \times \vec{E} + \rho\vec{g} \tag{26}$$

$$\bar{\bar{\sigma}} = \mu\left(\nabla\overrightarrow{u_1} + \nabla\overrightarrow{u_1}^T\right) - \frac{2}{3}\mu(\nabla.\overrightarrow{u_1})\bar{\bar{I}} \tag{27}$$

$$p = 0 \tag{28}$$

$$\overrightarrow{u_1} = \vec{0} \tag{29}$$

$$\bar{\bar{\sigma}}.\vec{n} = \vec{0} \tag{30}$$

$$\overrightarrow{u_1} = -\frac{2Q_v}{\pi} \times \frac{R_{nozzle}^2 - r^2 + \left(R_{nozzle}^2 - R_{cathode}^2\right) \times \log\left(\frac{r}{R_{nozzle}} - \frac{R_{nozzle}}{R_{cathode}}\right)}{R_{nozzle}^4 - R_{cathode}^4 + \frac{\left(R_{nozzle}^2 - R_{cathode}^2\right)^2}{\log\left(\frac{R_{nozzle}}{R_{cathode}}\right)}} \overrightarrow{e_z} \tag{31}$$

$$\overrightarrow{u_1}.\vec{t} = 0 \tag{32}$$

$$\overrightarrow{u_1}.\vec{n} = \frac{\partial \psi}{\partial t} \tag{33}$$

Fluid flow in melt pool (Ω_{al})

Similar to fluid flow in plasma, the following equations introduce mass conservation (34) and momentum conservation (35). The viscous stress tensor (36) is adapted to describe an incompressible fluid. The source term associated with momentum conservation is detailed in equation (37), including the Lorentz force, the Buoyancy force to account for the effect of the density gradient with the incompressible viscous stress tensor, and a Darcy force to model the mushy zone between the liquid and solid phases. A Dirichlet condition is defined by equation (40) on the boundaries of the domain, excluding the anode-plasma interface ($\partial\Omega \in (\partial\Omega_\mathrm{al} \cap \partial\Omega_\mathrm{as})$). Similar to equation (33), the normal velocity at the anode-plasma interface ($\partial\Omega \in \left(\partial\Omega_\mathrm{p} \cap \partial\Omega_\mathrm{al}\right)$) is imposed by equation (41), with ψ representing the axial position of this interface. On this same interface, a tangential force is applied by equation (39), associated with the surface tension gradient, more commonly known as the Marangoni effect.

$$\nabla.(\rho\overrightarrow{u_2}) = 0 \tag{34}$$

$$\rho\left(\frac{\partial \overrightarrow{u_2}}{\partial t} + (\overrightarrow{u_2}.\nabla)\overrightarrow{u_2}\right) = \nabla.\left(-p_2\bar{\bar{I}} + \bar{\bar{\sigma}}\right) + \vec{F} \tag{35}$$

$$\bar{\bar{\sigma}} = \mu\left(\nabla\overrightarrow{u_2} + \nabla\overrightarrow{u_2}^T\right) \tag{36}$$

$$\vec{F} = \vec{J} \times \vec{B} - \rho_{ref}\beta\left(T - T_{ref}\right)\vec{g} - C\frac{(1-fl)^2}{fl^3+B}\overrightarrow{u_2} \tag{27}$$

$$fl = \begin{cases} 0\ for\ t < T_s \\ \frac{T-T_s}{T_l-T_s}\ for\ T_s \leq T \leq T_l \\ 1\ for\ T > T_l \end{cases} \tag{38}$$

$$\bar{\bar{\sigma}}.\vec{t} = \mu\frac{\partial u_{1_T}}{\partial z} + \frac{\partial \gamma}{\partial r} \times \frac{\partial T}{\partial r} \tag{39}$$

$$\overrightarrow{u_2} = \vec{0} \tag{40}$$

$$\overrightarrow{u_2}.\vec{n} = \frac{\partial \psi}{\partial t} \tag{41}$$

Movement on the plasma-anode interface ($\partial\Omega_{al} \cap \partial\Omega_p$)

The variable ψ represents the vertical position of the interface. Helmholtz's equation (42) reflects the minimisation of the energies associated with surface tension, plasma surface pressure and gravitational potential energy. The surface tension coefficient is strongly increased when the temperature is lower than the melting temperature in order to avoid movements in the solid phase, as described by equation (43). Conservation of deformed volume is defined equation (44). A Dirichlet condition is imposed at the boundary of the moving interface ($\partial\Omega \in$ J) by equation (45).

$$\nabla_t.\left(\frac{\gamma^*}{\sqrt{1+\frac{\partial\psi^2}{\partial r^2}_T}}\right) = p_1 \tag{42}$$

$$\gamma^* = \gamma_l \times fl + \gamma_s \times (1 - fl) \tag{43}$$

$$\int \psi = 0 \tag{44}$$

$$\psi = 0 \tag{45}$$

Moving mesh ($\Omega \in \Omega_{ALE}$)

The axial displacement of the mesh is controlled by a modified form of the Laplace equation (46) to limit distortions in the mesh boundary layer at the plasma-anode interface ($\partial\Omega \in KJ$). A null Dirichlet condition is imposed at ($\partial\Omega \in$ PQ ∪ QO ∪ ON) to ensure continuity with the non-moving mesh by equation (47). At the interface ($\partial\Omega_{\mathrm{al}} \cap \partial\Omega_{\mathrm{p}}$), the axial displacement is equal to the solution of the previously presented Helmholtz equation (48).

$$\frac{\partial}{\partial z}\left(\frac{1}{z}\frac{\partial \phi}{\partial z}\right) = 0 \quad (46)$$

$$\phi = 0 \quad (47)$$

$$\phi = \psi \quad (48)$$

ANALYSIS OF HYPOTHESES

The main goal of this section is to justify and critically analyse the validity of our model assumptions which are based on Brochard work [14]. First, the problem is axisymmetric due to the geometry of the weld piece and the stationary torch. This assumption enables simplification of numerical resolution. However, it is difficult to reproduce it experimentally. As an example, it has been observed that light scratches on the electrode could disrupt the axisymmetry of the arc. Multiple assumptions associated with the arc are justified by the work of Delalondre et al. [24] :

- local thermodynamic equilibrium (LTE): homogenization of species temperatures, within the arc column except cathodic and anodic interfaces by using LTE-diffusion approximation involving modified electrical conductivity as described by Lowke [25];
- quasi-neutrality;
- magnetostatism;
- elimination of the electrical component of Lorentz force by considering quasi-neutrality hypotheses;
- Thomson's effect neglected; The Thomson effect, as reported in [4] is primarily dominant in the vicinity of the electrodes, particularly the cathode.
- simplified modelling of the anodic interface incorporating only a source term associated with electron absorption and not the anode fall [12], [26];
- plasma transparent and optically thin allowing the use of a net emission coefficient to model radiative losses;
- the impact of plasma radiation on electrode surfaces is not considered because it is assumed negligible for this specific configuration compared to other thermal phenomena.

The solving of fluid flow in the plasma is conditioned by the following assumptions:

- hydrodynamic continuity;
- laminar flow: for simplification the plasma is considered laminar. The justification of this assumption for this specific welding configuration involves a comparison with a turbulent model as conducted by Bauchire [27] or experimental observations in plasma;
- weakly compressible flow ($\mathrm{Ma} = 0.11 < 0.3$): the approximated sound velocity in plasma is calculated by assuming that it is a perfect gas $U_s = \sqrt{\frac{\gamma_g p}{\rho}} \approx \sqrt{\frac{1.4\times 101325}{2E-2}}$

The assumptions associated with the thermo-hydrodynamic of melt pool are:

- Laminar regime: The Reynolds number is 1076. It is calculated with the properties of the liquid metal used in simulation at 2000 K ($\mu = 3E-2\ Pa.s; \rho = 6725\ kg/m^3$), the maximum velocity obtained ($0.6\ m/s$) and the diameter of the melt pool ($8E-3$). This dimensionless number is not representative of the real problem. The viscosity of the fluid is artificially increased by thirty to be laminar for numerical simplification. Experimental observations confirm the surface turbulence of the flow.
- Incompressible flow ($\mathrm{Ma} = 0.0003 \ll 0.3$) : The calculation of this dimensionless number is performed with the same maximum velocity and the velocity of sound in the liquid metal is approximated to be identical than water at ambient temperature.
- The enthalpy of fusion is not taken into account because this phenomenon is negligible in the spot configuration on the behaviour of the flows in the melt pool, as shown by Cadiou [21].

Only the thermal effect of metal evaporation is considered. In the simulation, metallic vapours are considered to have no effect on plasma. This assumption is justified for a relatively short weld duration and low intensity. Numerical and experimental works such as Xiang et al. [28], Lago et al. [29] and Simon et al. [30] study their sensitivities.

MATERIAL PROPERTIES

Table 1 summaries the material properties associated with the tungsten cathode, the argon plasma and the 304L stainless steel anode. Equations are defined for density (51), heat capacity (54) and thermal conductivity (57). There are obtained from Kim et al. [23] for the liquid phase. The solid phase are experimentally characterised with:

- differential scanning calorimetry (LABSYS evo STA - Setaram);
- diffusivimeter (LFA 475/2/6 – Netzch);
- dilatometer (L75/20C – Linseis).

$$\rho_s = 8.04E3 - 4.62E-1 \times T + 1.69E-5 \times T^2 \quad (49)$$

$$\rho_l = 7.55E3 - 1.12E-1 \times T - 1.51E-4 \times T^2 \quad (50)$$

$$\rho = \rho_s \times (1 - fl) + \rho_l \times fl \quad (51)$$

$$Cp_s = 4.68E2 + 1.39E-1 \times T \quad (52)$$

$$Cp_l = 7.95E+2 \quad (53)$$

$$Cp = Cp_s \times (1 - fl) + Cp_l \times fl \quad (54)$$

$$\lambda_s = 1.31E+1 + 1.19E-2 \times T + 8.75E-7 \times T^2 - 3.72E-10 \times T^3 + 2.11E-14 \times T^4 - 6.49E-19 \times T^5 \quad (55)$$

$$\lambda_l = 1.51E+1 - 1.03E-4 \times T + 1.13E-6 \times T^2 - 2.36E-11 \times T^3 - 2.86E-14 \times T^4 \quad (56)$$

$$\lambda = \lambda_s \times (1 - fl) + \lambda_l \times fl \quad (57)$$

Table 1 Volume material properties.

	Cathode (Ω_c)	**Plasma** (Ω_p)	**Anode** ($\Omega_{al} \cup \Omega_{as}$)
ρ	$17800\ kg/m^3$		*Figure 4 and* (51)
C_p	$132\ J/(kg.K)$	[31]	*Figure 4 and* (54)
λ	[32]		*Figure 4 and* (57)
ϵ	$\emptyset$	[29]	$\emptyset$
μ	$\emptyset$	[31]	$\begin{cases} 1E4\ for\ T < T_f \\ 3E-2\ for\ T > T_f \end{cases}$
σ	[23]	$\sigma_{tungsten}$ [23] *near cathode* σ_{argon} [31] $7.7E5\ S/m$ *near anode*	$7.7E5\ S/m$
μ_r	1	1	1

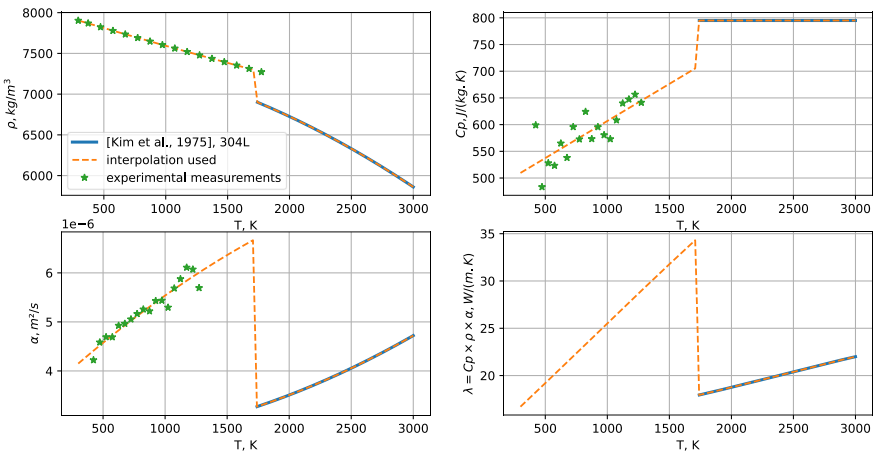

Fig. 4 Thermophysical properties of 304L

Table 2 presents the constants associated specifically with metal. The surface tension gradient with temperature is a thermo-physical parameter which determines the surface flow in the melt pool (Marangoni effect). This value is extremely sensitive to the activity of the surface-active elements. It can vary strongly for the same stainless grade. The effect of this parameter is not the subject of this article that is why its sensitivity is not studied. For this work, two values are set to study two distinct melt pool configurations and generalise the results of this study:

- $\frac{\partial \gamma}{\partial T} = +2.1E-4\ N/(m.K)$: forming a deep and narrow melt pool;
- $\frac{\partial \gamma}{\partial T} = -2.1E-4\ N/(m.K)$: forming a shallow and large melt pool.

The properties associated with cathode-plasma and anode-plasma interfaces are chosen by Hsu et al. [1]. Φ_e and ϕ_c are determined by inverse method with pyrometric measurement of the electrode surface during welding. The uncertainty associated with this single measurement is not estimated, which justifies the next sensitivity study. ϕ_a is based on experimental measurements performed on $Fe-\alpha$. It is observed and demonstrated by Yoshitake [33] that multiple parameters like alloy elements and atomic organisation can strongly influence this value at solid state. The influence of the phase change is not studied. It is therefore also not possible to estimate the variability of this value.

Table 2 Physical constants.

Physical constant	Value
T_s	$1708\ K$
T_l	$1740\ K$
C/B	$1E9$
ρ_{ref}	$6874\ kg/m^3$
β	$1E-4\ K^{-1}$
T_{ref}	$1723\ K$
γ	$1.5\ N/m$
h_{conv}	$10\ W/(m^2.K)$
ϵ_c	0.4
ϵ_a	$\begin{cases} 0.7\ if\ T > \frac{T_l+T_s}{2} \\ 0.4\ if\ T < \frac{T_l+T_s}{2} \end{cases}$
ϕ_e	$2.63\ V$
V_i	$15.68\ V$
ϕ_c	$4.52\ V$
ϕ_a	$4.7\ V$

NUMERICAL RESOLUTION

The used mesh consists of tetrahedral elements with linear shape functions for all the physics except Helmholtz equation for which it is quadratic. A boundary layer mesh is chosen for the axis of revolution and electrode interfaces where strong unidirectional gradients are present. The mesh is divided into different areas with different sizes detailed in figure 5. A sensitivity on the mesh size is conducted (see figure 6) to its effect on shear, temperature, pressure, current density at the plasma-anode interface, and velocity, pressure temperature on the axisymmetry axis. The time step and minimum convergence criteria are constants for this study. It is observed that a coarse mesh leads to an underestimation of shear due to an incorrect description of flows at the interface. A satisfactory convergence is observed for a mesh size

equal to 0.15 *mm* without too high calculation time. A finer mesh than 0.07 *mm* results in numerical instability.

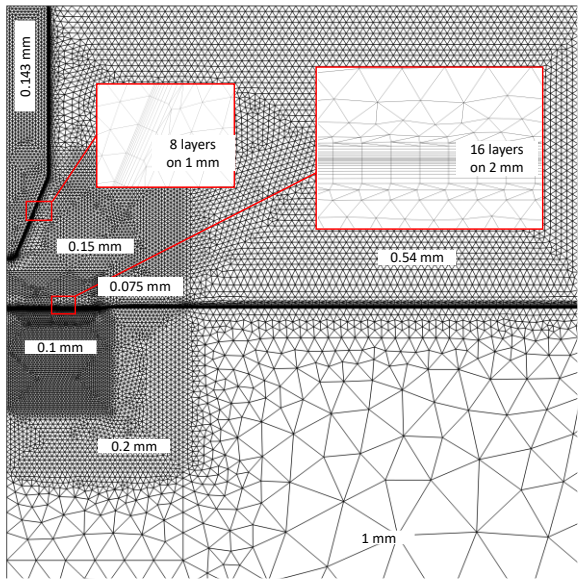

Fig. 5 Mesh sizes

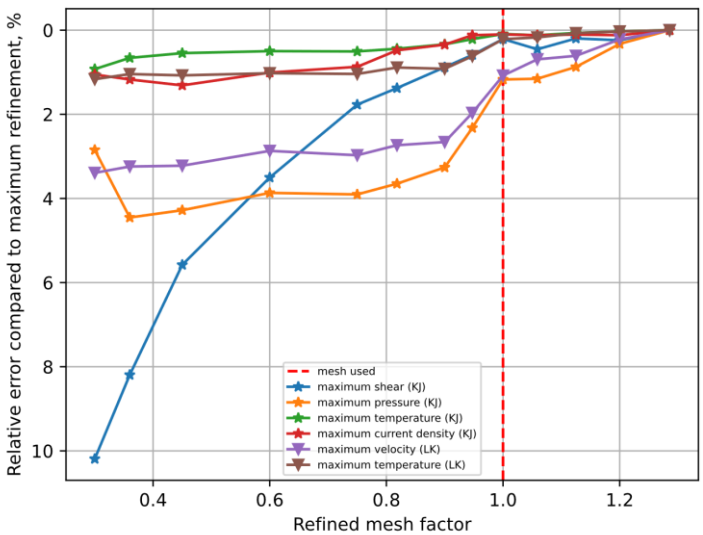

Fig. 6 Numerical convergence of the mesh

A segregated solver is used with four steps:

- fluid flow, heat transfer in plasma and electromagnetism;
- fluid flow and heat transfer in melt pool;
- moving interface equations;
- moving mesh equation.

The backward differentiation formula (BDF) of second order is used with Anderson acceleration. Simulation of a weld at 150 A with a mesh of 146073 degrees of freedom and 8 cores (Intel® Xeon®W-2295 CPU @3.00Ghz) generates a computation time equals to 7 hours and 36 minutes. The dissociation of the viscous stress tensor of plasma and melt pool leads to a reduction in calculation time by a factor of five. This approach also improves numerical stability. The error criterion used is defined by equation (58) which consists in evaluating iterative stability with M the number of fields, N_j the number of degrees of freedom for the field j, W_j the scale and $U_{i,j}$ the solution vector. The calculation is iterated for all variables as long as this relative error is less than 0.1%.

$$err = \sqrt{\frac{1}{M}} \sqrt{\sum_{j=1}^{M} \frac{1}{N_j} \sum_{i=1}^{N_j} \left(\frac{\left| U_{i,j_t} - U_{i,j_{t-\Delta t}} \right|}{\max(|U_{i,j_t}|)} \right)^2} \tag{58}$$

NUMERICAL ANALYSIS

GENERAL OVERVIEW

Figures 7 and 8 provide a brief overview of the numerical results obtained by this simulation at the melt pool and the arc scale with an intensity equal to $150\ A$ and a weld duration of $10\ s$.

The image on the left of figure 7 shows the temperature field. The tungsten electrode is heated to a temperature of 3600 K. Heating is limited by thermionic emission, which helps to reduce the effect of ion neutralisation. In the plasma, the temperature rises to 16,000 K just below the cathode. In this state, the argon is locally strongly ionized to the first and second degrees. The mechanisms associated with this heating are mainly the Joule effect and, and to a lesser extent, interfacial phenomena. Dissipation occurs through radiation and conduction to the surrounding domains. After stabilisation, the total voltage including the anode and cathode drop is equal to 10.6 V. The anode is partially melted by the heat transmitted by the plasma and the absorption of electrons. The temperature, in this area, reaches a maximum of 2600 K due to thermal pumping associated with vaporization enthalpy. The associated dissipation is mainly through radiation and convection.

The image on the middle of figure 7 shows the velocity fields. In the plasma, the flows are mainly axial, with very strong gradients between the cathode and the anode. The maximum velocity is equal to 160 m/s, due to the action of Lorentz forces and thermal expansion of the fluid. The flows generate an overpressure of 500 Pa at the anode-plasma interface. This causes a deformation of the interface equal to 0.25 mm. This deformation leads to a modification of

the flows in the plasma and the melt pool. In the anode, the liquid zone is in motion mainly due to the action of surface shear and the Marangoni effect at the anode-plasma interface, creating a very large axial gradient. The maximum velocity in this configuration is 0.16 m/s. This value is lower than in the plasma, but the Reynolds number associated is 6.7 times higher due to differences in fluid properties and associated sizes. The flows in the plasma and the melt pool are consequently very different.

The image on the right of figure 7 shows the electric potential field and the electric streamlines in the resolution domain. The potential difference is mainly located in the plasma, with a potential difference of 4.6 V. In addition, interfacial phenomena result in a total difference of 11 V. The streamlines are influenced by the cathode geometry and the deformation of the anode-plasma interface. A strong modification of this interface at high intensity implies a deviation of the electric field at the peripheral of the melt pool, leading to a change in the distribution of Lorentz forces in the melt pool and electron absorption at the surface.

The time-dependent calculation improves the understanding of the phenomena involved in the formation of the melt pool. Figure 8 shows the time evolution of the velocity and temperature fields with the temperature derivative of the surface coefficient equal to $2.1 \, . \, 10^{-4}$ N/(m.K). At 2 s the melt pool has two vortices. The first closest to the axis is centrifugal due to the predominance of the shear compared to the Marangoni effect. Away from the axis, the shear is reduced, allowing the action in the other direction of Marangoni to generate a second centripetal vortex. By increasing the welding time, the width of the melt pool is also increased, contributing to the predominance of the Marangoni effect. This leads to the formation of a single centripetal vortex. This example illustrates the complexity of the kinematics associated with thermo-hydrodynamic movements, justifying the time-dependent calculation.

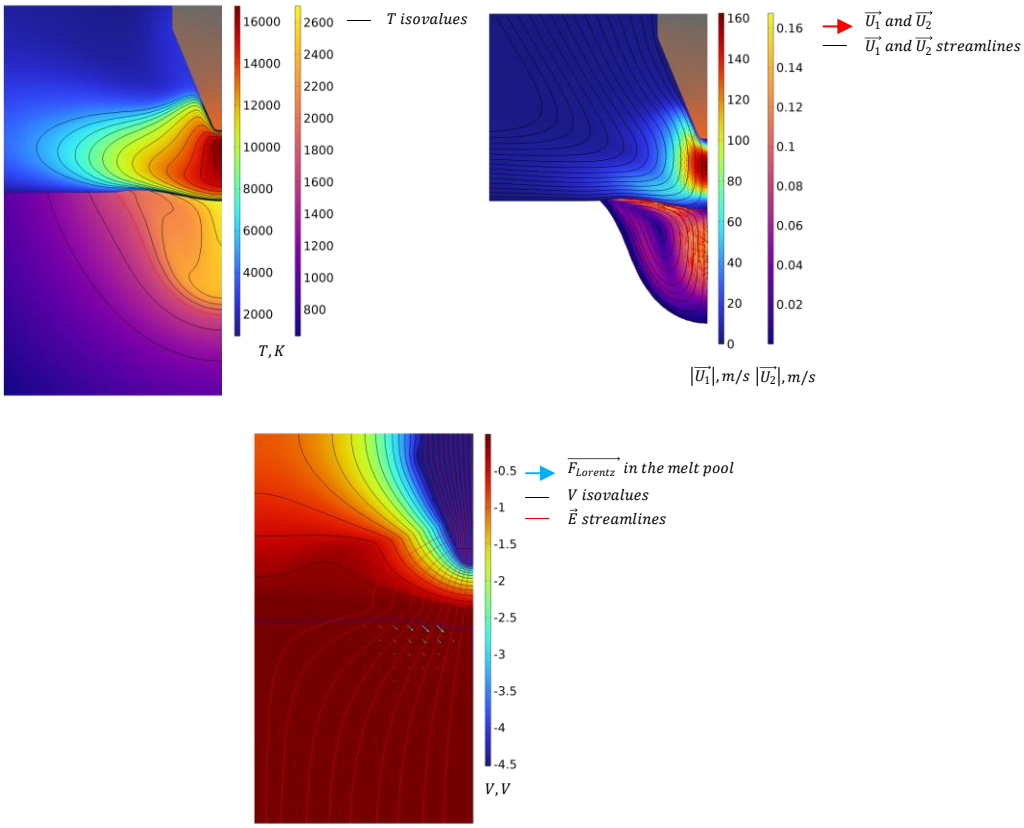

Fig. 7 Temperature, velocities and electric field

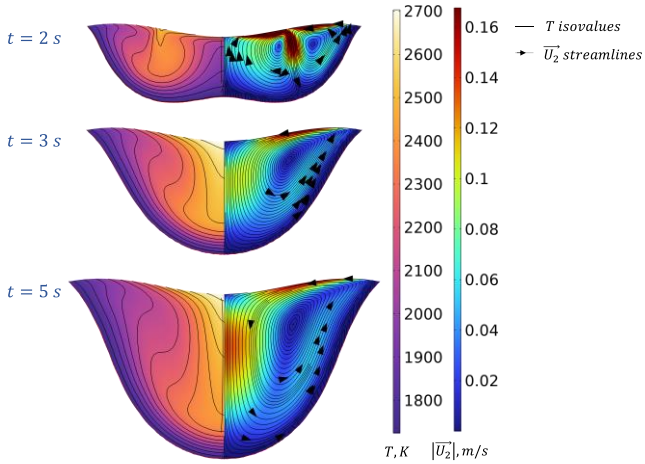

Fig. 8 Time evolution of temperature and velocity fields into the melt pool

ENERGY BALANCE

An energy balance is conducted in the cathode, the plasma, and the anode (see figure 9) for a welding duration and an intensity equal to 10 seconds and 150 A. The interest is to quantify the thermal contribution of all the phenomena at the scale of the process. At the end of the welding duration, the cathode has reached thermal equilibrium. The main contribution to heating is the ion neutralization at its surface (89.2%). Most of the dissipation is associated with the electron emission (61.7%) and to a lower but not negligible proportion with conduction at the top (34.9%). In simulation, this dissipation mechanism is simplified by imposing a temperature of $300\,K$ at the stick-out length. Experimentally, the tungsten electrode is cooled by the contact tube $13\,mm$ higher and by forced convection due to the flow of the cold shielding gas in the nozzle. This simplification is justified by the localisation of the thermal gradient at the tip of the cathode. In the plasma, the Joule effect is the phenomenon responsible for the heat input. This heat is redistributed by conduction to 10.8% to the cathode, 76.8% to the anode due to the direction of the fluid flows and 11.4% of the heat is dissipated by radiation with the net emission approach. In the anode, the heat input is 3.6 times higher than the dissipation. The stationary state is reached after approximately $100\,s$ in this configuration. The contribution is firstly associated with plasma conduction (41.4%) and electron absorption (58.3%). The heat generated by this last phenomenon is highly dependent of the work output of the anode (ϕ_a) but this value is not well known. According to the literature, it depends on multiple factors including the atomistic structure of the argon and stainless steel at the interface [33].This fact greatly justifies the need to realise a sensitivity study of the effect of material parameters. From this multiple information, it is possible to calculate the energy efficiency of the arc by the equation (59) from Nahed et al. [16]. It is

equal to 75.64%, this is consistent with literature values from Nestor et al. [34], Giedt et al. [35], Dupont et al. [36] and Smartt et al. [37]. These values range between 60 and 80% for different arc height and cathode sharpening but at the same intensity.

$$\eta = \frac{s_{cond-anode}+s_{IAP}}{s_{IAP}+s_{ICP}+U\times I} \tag{59}$$

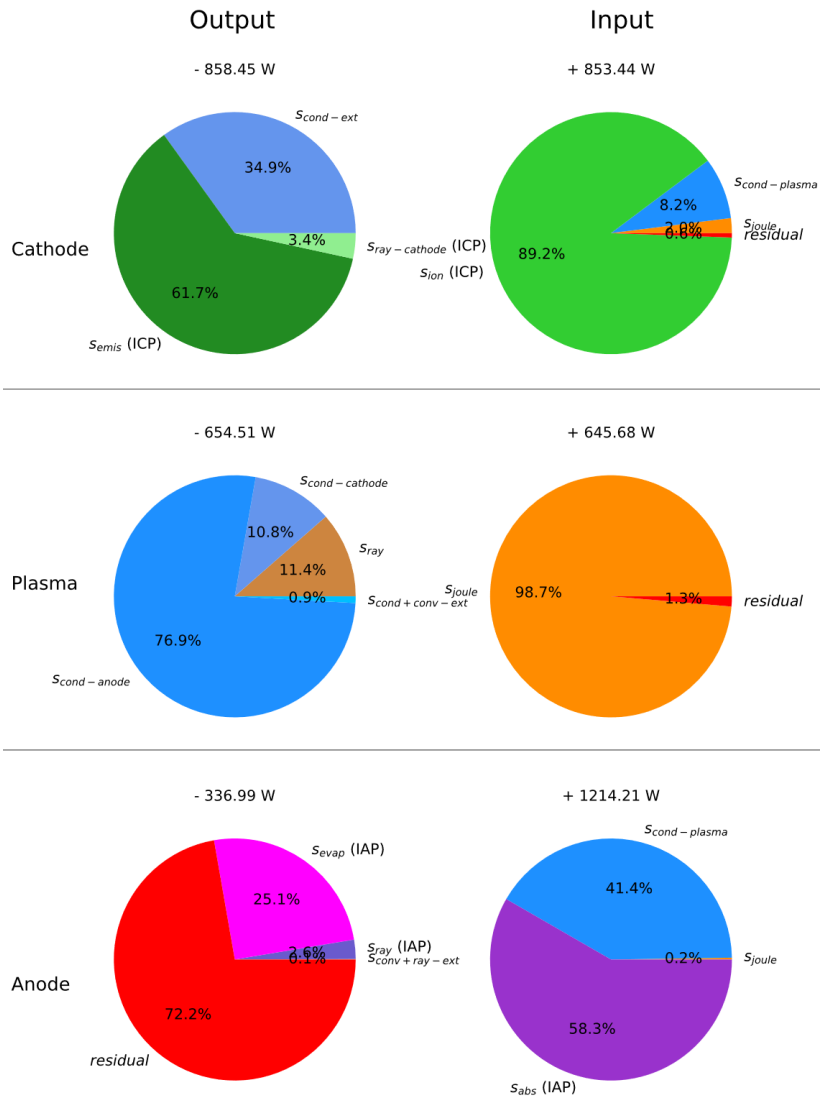

Fig. 9 Energy balance of the arc model

EFFECT OF THE ARC ON THE MELT POOL

The influence of the electrical arc over the melt pool is generated by : the heat flux, the shear, the arc pressure and the current density. At $150\,A$, the heat flux and the shear are the predominant phenomena. The objective of this part is to evaluate their influence on the behaviour of the melt pool for a variation of $\pm 10\%$. The evolution of the geometry of the melt pool is studied for two thermocapillary coefficients to generalise this study

Figure 10 illustrates the evolution of the fusion isotherm for a wider, shallower melt pool ($\frac{\partial \gamma}{\partial T} < 0$), and a narrower, deeper melt pool ($\frac{\partial \gamma}{\partial T} > 0$). Table 3 contains the relative differences associated with the dimensions of the melt pool. It is observed that the direction of application of the Marangoni effect has a significant effect on the influence of heat and shear.

The first consequence of increasing the incident heat flux is an approximate 23% increase in the melt pool volume, regardless the sign of $\partial\gamma/\partial T$. However, the shape does not change uniformly. For $\frac{\partial \gamma}{\partial T} > 0$, only the width is affected, whereas for $\frac{\partial \gamma}{\partial T} < 0$, both the width and depth increase.

The action of the shear is more complex due to its interdependence with the Marangoni effect. For $\frac{\partial \gamma}{\partial T} > 0$, the directions of the shear and the Marangoni effect are opposite, and the magnitude of the Marangoni effect is greater than that of the shear. In this case, an increase in the shear leads to a decrease in the total radial stress, which reduces convective movements within the melt pool and, consequently, its volume. Only the depth is affected ; the width is less sensitive to internal convection because it is strongly limited by conduction in the solid part. For $\frac{\partial \gamma}{\partial T} < 0$, the directions of the shear and the Marangoni effect are the same, making the total radial stress less sensitive to variations in the shear. Therefore, the shape of the melt pool is only slightly affected in this configuration.

The main conclusion of this little study is that these two terms can have a significant impact on the morphology of the melt pool. These results fully justify the need to improve the understanding of the influence of the material parameters of the arc model.

Table 3 Relative differences generated by a 10% change in shear and heat.

	$\frac{\partial \gamma}{\partial T} = +2.1E-4\ N/(m.K)$		$\frac{\partial \gamma}{\partial T} = -2.1E-4\ N/(m.K)$	
Characteristic	**Shear**	**Heat**	**Shear**	**Heat**
Width	0.0%	+4.8%	+0.7%	+7.7%
Depth	−5.8%	+12.2%	−0.3%	+7.2%
Volume	−6.1%	+23.7%	+1.9%	+22.5%
$\frac{\text{Width}}{\text{Depth}}$	+5.9%	−7.5%	+1.0%	+0.5%

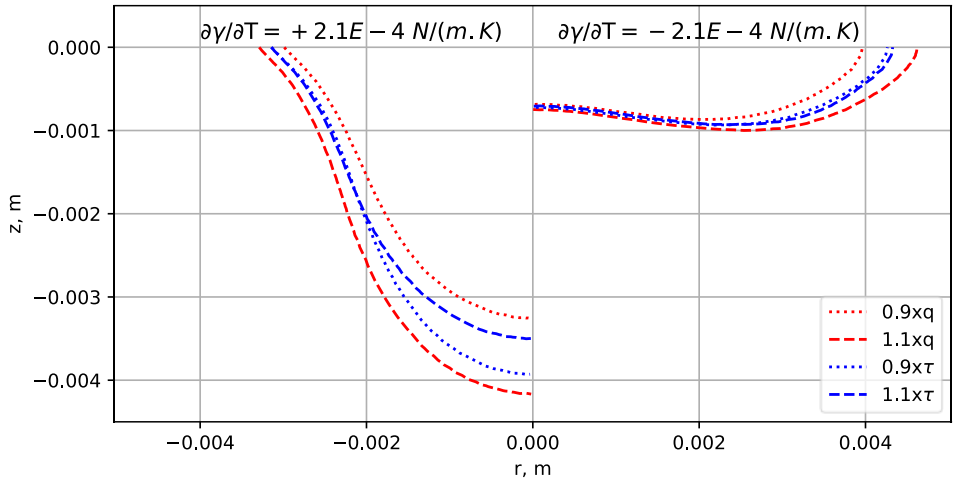

Fig. 10 Fusion isotherms with shear and heat variations for two Marangoni configurations

SENSITIVITY OF ARC MATERIAL PROPERTIES

The magneto-thermo-hydrodynamic simulation of the arc involves multiple material parameters. Some of them are very difficult to characterise, for example the thermophysical properties ionised argon ($\lambda, \rho, C_p, \sigma, \epsilon, \mu$). Tanaka et al. [12], Brochard [14], Traidia et al. [15], Cadiou et al. [21] and Nahed et al. [16] have used the same data from Boulos et al. [31]. These values are determined by a thermodynamic model for absolutely pure argon. The applicability of these data is therefore questionable because, experimentally, this is not the case. Metal species from anode fusion and cathode degradation are present in small quantities within the arc participating to modify these properties as shown for example by Zhao et al. [38]. Also, the properties associated with electro-magneto-thermal interfacial phenomena: ϕ_a, ϕ_c and ϕ_e are little known. These three parameters are obtained by inverse method with a complex temperature measurement of the cathode surface through the arc during welding by Hsu et al. [1].

Failing to be able to characterize or known these properties accurately, simulation can be used to identify influential parameters. The properties in table 4 are studied. An individual variation of $\pm 10\%$ is applied to study the effect of the following quantities at the anode-plasma interface: heat flux, shear and pressure. The sensitivity of the material properties on the maxima of the three quantities is synthesised by figure 11. The main conclusion is the significant importance of the thermophysical properties of the shielding gas compared to ϕ_e, ϕ_a and ϕ_c. The shear is the variable most impacted by the variability of material properties. A little change leads to a modification of flow into the melt pool as demonstrated in the previous part. This study confirms that the material properties of the arc model can have a

significant impact on the incident terms at the anode-plasma interface. The lack of knowledge of these properties can be a limit to the predictivity of the model.

The main limit of this approach is to achieve a simple proportional variation of $\pm 10\%$. The choice of this variation value is questionable. Variations of 40% are for example present in the literature for ϕ_a, while for σ_W is less than 5%. It would be relevant to complete this study with a bibliographic review of the totality of material parameters present in the literature to estimate their dispersions. The second weakness is to limit this study to the material properties of the arc. Indeed, the melt pool is also extremely sensitive to the properties of liquid metal in particular the surface tension coefficient responsible for the Marangoni effect.

Table 4 Arc model material parameters used for sensitivity.

Location	Symbol	Definition
Cathode (Tungsten)	λ_W	Thermal conductivity
	ρ_W	Density
Cathode-plasma interface	h_{ICP}	Thickness of the cathodic zone
	V_i	Ionisation potential
	ϕ_e	Effective work function at the cathode interface
	ϕ_c	Work function at the cathode interface
	ϵ_c	Emissivity of the cathode surface
Plasma (Argon)	λ_{Ar}	Thermal conductivity
	ρ_{Ar}	Density
	$C_{p_{Ar}}$	Heat capacity at constant pressure
	μ_{Ar}	Dynamic viscosity
	σ_{Ar}	Electrical conductivity
	ϵ_{Ar}	Net emission coefficient
Plasma-anode interface	h_{IAP}	Thickness of the anodic zone
	ϕ_a	Work function at the interface
	ϵ_a	Emissivity of the anode surface
Anode (304L)	λ_{304L}	Thermal conductivity
	ρ_{304L}	Density
	σ_{304L}	Electrical conductivity
	ϵ_{radsol}	Net emissivity
Plasma (Argon)	λ_{Ar}	Thermal conductivity
	ρ_{Ar}	Density
	$C_{p_{Ar}}$	Heat capacity at constant pressure
	h_{conv}	Convective heat transfer coefficient

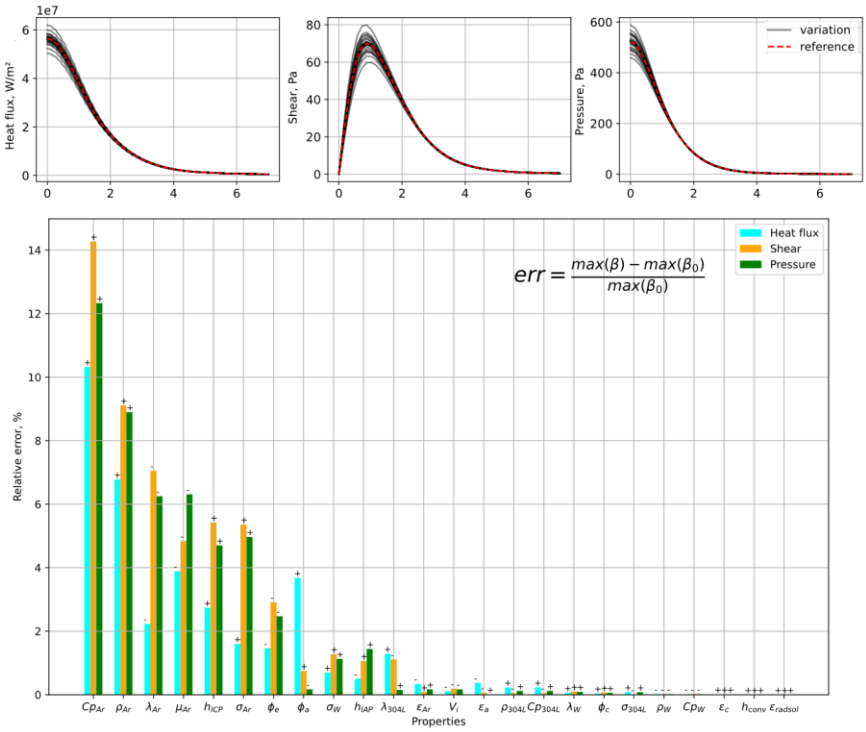

Fig. 11 Sensitivity of material properties at the anode-plasma interface for an individual variation of 10%

CONCLUSION

The first part of this article is a presentation as exhaustive as possible of the magneto-thermo-hydrodynamic simulation of the TIG process with arc-melt pool coupling and surface deformation in spot configuration.

This simulation highlights the influence of the arc on the melt pool and to evaluate the sensitivity of material properties on arc behaviour. The most sensitive properties are λ, ρ, C_p and μ of argon. For instance, a 10% increase in C_p can result in an increase of more than 23% in the melt pool volume. Unfortunately, it is not possible to justify the uncertainties associated with these parameters because they are determined by thermodynamic calculations. The metal vapours can strongly influence these properties. According to mixing law from Wilke et al. [39] the addition of 1% iron results in a 25% decrease in μ. However, this simulation does not include the consideration of metallic vapours, this study clearly illustrates the importance of considering this phenomenon. The work function at the anode-plasma is also little known for liquid metal and proportionally influences the volume of the melt pool. It is therefore very important to improve the knowledge of this value to have a predictive model.

The perspectives associated with this work are to continue these sensitivities at the scale of the melt pool, with a focus on surface tension coefficient which is the predominant phenomenon. Another perspective is to compare the numerical and experimental results in order to evaluate the predictivity of the model with a variation in intensity.

APPENDIX

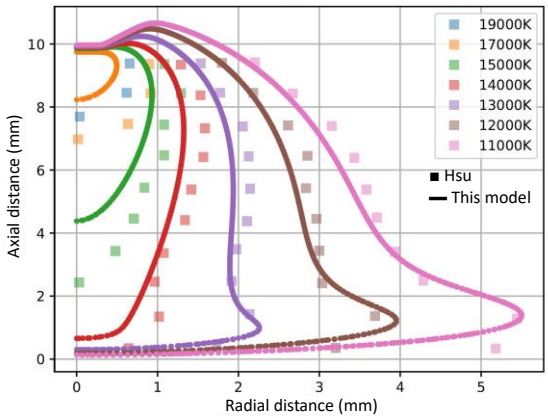

Fig. 12 Comparison of plasma temperature measured by Hsu et al. [1] for argon, an intensity of 200 A and an arc length of 10 mm

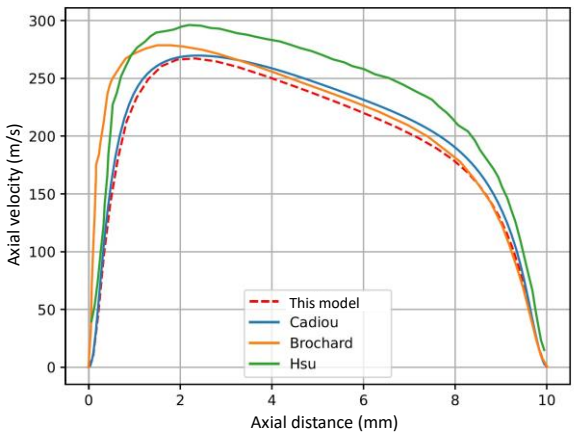

Fig. 13 Comparison of the axial velocities within the plasma obtained in simulation obtained by Cadiou et al. [21], Brochard et al. [14] and Hsu et al. [1] for argon, an intensity of 200 A and an arc length of 10 mm

References

[1] K. C. HSU, K. ETEMADI and E. PFENDER: 'Study of the free-burning high-intensity argon arc', *Journal of Applied Physics*, vol. 54, no. 3, pp. 1293-1301, Mar. 1983, doi: 10.1063/1.332195.

[2] J. MCKELLIGET and J. SZEKELY: 'Heat transfer and fluid flow in the welding arc', *Metallurgical Transactions A*, vol. 17, pp. 1139-1148, 1986.

[3] J. J. LOWKE, P. KOVITYA and H. P. SCHMIDT: 'Theory of free-burning arc columns including the influence of the cathode', *J. Phys. D: Appl. Phys.*, vol. 25, no. 11, p. 1600, Nov. 1992, doi: 10.1088/0022-3727/25/11/006.

[4] A. VELÁZQUEZ-SÁNCHEZ, A. DELGADO-ÁLVAREZ, P. F. MÉNDEZ, A. B. MURPHY and M. A. RAMÍREZ-ARGÁEZ: 'Dominant heat transfer mechanisms in the GTAW plasma arc column', *Plasma Chemistry and Plasma Processing*, vol. 41, no. 5, pp. 1497-1515, 2021.

[5] G. OREPER, T. EAGAR and J. SZEKELY: 'Convection in arc weld pools', *Welding Journal*, vol. 62, no. 11, pp. 307-312, 1983.

[6] J. SZEKELY: *Transport phenomena in welds with emphasis on free surface phenomena*, 1989.

[7] T. ZACHARIA, S. DAVID, J. VITEK and T. DEBROY: 'Weld pool development during GTA and laser beam welding of type 304 stainless steel, Part II–experimental correlation', *Welding Journal*, vol. 68, no. 12, pp. 510s-519s, 1989.

[8] R. C. CHOO and J. SZEKELY: 'The effect of gas shear stress on Marangoni flows in arc welding', *Welding Journal*, vol. 70, no. 9, pp. 223-233, 1991.

[9] T. DEBROY and S. DAVID: 'Physical processes in fusion welding', *Reviews of Modern Physics*, vol. 67, no. 1, p. 85, 1995.

[10] M. LIN and T. EAGAR: 'Influence of surface depression and convection on arc weld pool geometry', *Transport Phenomena in Materials Processing*, vol. 10, pp. 63-69, 1983.

[11] W.-H. KIM and S.-J. NA: 'Heat and fluid flow in pulsed current GTA weld pool', *International Journal of Heat and Mass Transfer*, vol. 41, no. 21, pp. 3213-3227, 1998.

[12] M. TANAKA, H. TERASAKI, M. USHIO and J. J. LOWKE: 'A unified numerical modeling of stationary tungsten-inert-gas welding process', *Metall Mater Trans A*, vol. 33, no. 7, pp. 2043-2052, July 2002, doi: 10.1007/s11661-002-0036-2.

[13] A. B. MURPHY, M. TANAKA, K. YAMAMOTO, S. TASHIRO, J. J. LOWKE and K. OSTRIKOV: 'Modelling of arc welding: The importance of including the arc plasma in the computational domain', *Vacuum*, vol. 85, no. 5, pp. 579-584, 2010.

[14] M. BROCHARD: *Modèle couplé cathode-plasma-pièce en vue de la simulation du procédé de soudage à l'arc TIG*, These de doctorat, Aix-Marseille 1, 2009. Accessed: Dec. 09, 2024. [Online]. Available: https://theses.fr/2009AIX11006

[15] A. TRAIDIA and F. ROGER: 'Numerical and experimental study of arc and weld pool behaviour for pulsed current GTA welding', *International Journal of Heat and Mass Transfer*, vol. 54, no. 9, pp. 2163-2179, Apr. 2011, doi: 10.1016/j.ijheatmasstransfer.2010.12.005.

[16] C. NAHED, S. GOUNAND and M. MEDALE: 'A numerical study of the effects of cathode geometry on tungsten inert gas type electric arcs', *International Journal of Heat and Mass Transfer*, vol. 182, p. 121923, Jan. 2022, doi: 10.1016/j.ijheatmasstransfer.2021.121923.

[17] A. EBRAHIMI, C. R. KLEIJN and I. M. RICHARDSON: 'A simulation-based approach to characterise melt-pool oscillations during gas tungsten arc welding', *International Journal of Heat and Mass Transfer*, vol. 164, p. 120535, 2021.

[18] D. WU, J. HUANG, L. KONG, X. HUA and M. WANG: 'Coupled mechanisms of arc, weld pool and weld microstructures in high speed tandem TIG welding', *International Journal of Heat and Mass Transfer*, vol. 154, p. 119641, 2020.

[19] M. BAEVA, Y. CRESSAULT and P. KLOC: 'Comparative Studies on the Radiative Heat Transfer in Arc Plasma and Its Impact in a Model of a Free-Burning Arc', *Plasma*, vol. 7, no. 3, pp. 631-650, 2024, doi: 10.3390/plasma7030033.

[20] X. WANG, S. TASHIRO, M. TANAKA and A. B. MURPHY: 'Numerical Investigation of the Iron and Oxygen Transport in Arc Plasma During an Activated Tungsten Inert Gas Welding Process', *Plasma Chemistry and Plasma Processing*, vol. 44, no. 1, pp. 25-45, 2024.

[21] S. CADIOU, M. COURTOIS, M. CARIN, P. LE MASSON, L. GUILMOIS and P. PAILLARD: 'Development of a two-dimensional axial symmetry model for wire arc additive manufacturing', in *Mathematical Modelling of Weld Phenomena 12. Verlag der Technischen Universität Graz*, 2018. doi: https://doi.org/10.3217/978-3-85125-615-4-56.

[22] T. DEBROY, S. BASU and K. MUNDRA: 'Probing laser induced metal vaporization by gas dynamics and liquid pool transport phenomena', *Journal of Applied Physics*, vol. 70, no. 3, pp. 1313-1319, Aug. 1991, doi: 10.1063/1.350358.

[23] C. S. KIM: 'Thermophysical properties of stainless steels', Argonne National Lab., Ill. (USA), ANL-75-55, Sept. 1975. doi: 10.2172/4152287.

[24] C. DELALONDRE and O. SIMONIN: 'Modelling of high intensity arcs including a non-equilibrium description of the cathode sheath', *J. Phys. Colloques*, vol. 51, no. C5, pp. C5-206, Sept. 1990, doi: 10.1051/jphyscol:1990524.

[25] J. J. LOWKE and M. TANAKA: 'LTE-diffusion approximation' for arc calculations', 2006, doi: 10.1088/0022-3727/39/16/017.

[26] A. TRAIDIA: *Multiphysics modelling and numerical simulation of GTA weld pools*, 2011.

[27] J. M. BAUCHIRE, J. J. GONZALEZ and A. GLEIZES: 'Modeling of a DC Plasma Torch in Laminar and Turbulent Flow', 1997, doi: https://doi.org/10.1023/A:1021847113956.

[28] J. XIANG, F. F. CHEN, H. PARK, K. TANAKA, M. SHIGETA, M. TANAKA and A. B. MURPHY: 'Numerical study of the metal vapour transport in tungsten inert-gas welding in argon for stainless steel', *Applied Mathematical Modelling*, vol. 79, pp. 713-728, Mar. 2020, doi: 10.1016/j.apm.2019.11.001.

[29] F. LAGO, J. J. GONZALEZ, P. FRETON and A. GLEIZES: 'A numerical modelling of an electric arc and its interaction with the anode: Part I. The two-dimensional model', *J. Phys. D: Appl. Phys.*, vol. 37, no. 6, p. 883, Feb. 2004, doi: 10.1088/0022-3727/37/6/013.

[30] M. S. SIMON: *On the mechanism of evaporation-determined arc-cathode coupling in GMA welding*, PhD Thesis, RWTH Aachen University, 2021.

[31] M. I. BOULOS, P. FAUCHAIS and E. PFENDER: *Thermal Plasmas: Fundamentals and Applications*, Springer Science & Business Media, 2013.

[32] C. S. WU, J. CHEN and Y. M. ZHANG: 'Numerical analysis of both front- and back-side deformation of fully-penetrated GTAW weld pool surfaces', *Computational Materials Science*, vol. 39, no. 3, pp. 635-642, May 2007, doi: 10.1016/j.commatsci.2006.08.018.

[33] M. YOSHITAKE: *Work Function and Band Alignment of Electrode Materials: The Art of Interface Potential for Electronic Devices, Solar Cells, and Batteries*. in NIMS Monographs, Tokyo: Springer Japan, 2021. doi: 10.1007/978-4-431-56898-8.

[34] O. H. NESTOR: 'Heat Intensity and Current Density Distributions at the Anode of High Current, Inert Gas Arcs', *Journal of Applied Physics*, vol. 33, no. 5, pp. 1638-1648, May 1962, doi: 10.1063/1.1728803.

[35] W. GIEDT, L. TALLERICO and P. FUERSCHBACH: 'GTA welding efficiency: calorimetric and temperature field measurements', *Weld. J.*, vol. 68, p. 28, 1989.

[36] J. N. DUPONT and A. MARDER: 'Thermal efficiency of arc welding processes', *Welding Journal-Including Welding Research Supplement*, 1995.

[37] H. B. SMARTT, J. A. STEWART and C. J. EINERSON: 'Heat transfer in gas tungsten arc welding', EG and G Idaho, Inc., Idaho Falls (USA), EGG-J-01586; CONF-8510160-19, May 1986. Accessed: Dec. 09, 2024. [Online]. Available: https://www.osti.gov/biblio/5500789

[38] G. Y. ZHAO, M. DASSANAYAKE and K. ETEMADI: 'Numerical Simulation of a Free-Burning Argon Arc with Copper Evaporation from the Anode', *Plasma Chemistry and Plasma Processing*, vol. 10, 1990.

[39] C. R. WILKE: 'A Viscosity Equation for Gas Mixtures', *The Journal of Chemical Physics*, vol. 18, no. 4, pp. 517-519, Apr. 1950, doi: 10.1063/1.1747673.